Improved contact angle measurement in multiphase lattice Boltzmann

Xing-Guo Zhong(钟兴国), Yang-Sha Liu(刘阳莎), Yi-Chen Yao(姚怡辰), Bing He(何冰)[†], and Bing-Hai Wen(闻炳海)[‡]

College of Computer Science and Engineering, Guangxi Normal University, Guilin 541004, *China*

(Received 4 August 2022; revised manuscript received 10 October 2022; accepted manuscript online 21 October 2022)

Contact angle is an essential parameter to characterize substrate wettability. The measurement of contact angle in experiment and simulation is a complex and time-consuming task. In this paper, an improved method of measuring contact angle in multiphase lattice Boltzmann simulations is proposed, which can accurately obtain the real-time contact angle at a low temperature and larger density ratio. The three-phase contact point is determined by an extrapolation, and its position is not affected by the local deformation of flow field in the three-phase contact region. A series of simulations confirms that the present method has high accuracy and gird-independence. The contact angle keeps an excellent linear relationship with the chemical potential of the surface, so that it is very convenient to specify the wettability of a surface. The real-time contact angle measurement enables us to obtain the dynamic contact angle hysteresis on chemically heterogeneous surface, while the mechanical analyses can be effectively implemented at the moving contact line.

Keywords: contact angle measurement, contact angle hysteresis, mechanical analysis, lattice Boltzmann method

PACS: 47.11.–j, 05.50.+q, 47.61.Jd, 47.55.np **DOI:** 10.1088/1674-1056/ac9cbd

1. Introduction

Contact angle usually assesses the wettability of a solid surface.[1] The contact angle measurement is of utmost importance in many studies that are influenced by the surface properties. Measurement methods have different applications in experiment[2–18] and simulation,[19–28] such as contact line moving,[2] wetting behaviors,[3] capillary phenomena[4] or diffuse-interface simulations.[22–26]

There are three kinds of methods to measure contact angles in experiment: the sessile drop, the Wilhelmy balance, and the Washburn capillary rise methods.[5] The initial measurement is the sessile drop method, which is a direct measurement method. This method measures the contact angle by capturing cross-section of the sessile droplet on the substrate with a high-resolution camera.[6] Extrand and Kumagai studied contact angle hysteresis on different surface materials by the inclined plate method that is a variant of the sessile drop method.[7] Wilhelmy proposed a new indirect measurement method.[8] In this method, thin sheet of metal coated with the sample is immersed in the liquid, and its weight and perimeter of infiltration are calculated to measure the contact angle indirectly.[8] The method can be used to measure the contact angle hysteresis by immersing or pulling the thin sheet from the liquid in uniform velocity.[9] The Wilhelmy balance method is accurate and objective, contrasting with the sessile drop method. In the Washburn capillary rise method,[10] contact angle can be also calculated by measuring the height at which the liquid rises in a capillary that is filled with sample powder. However, the experimental measurements are usually complex and time-consuming.[11–18]

Numerical simulation has become an effective tool to investigate wetting phenomena, as it has a low cost and can capture more details.[19,20] In the early stage, some scholars used a goniometer to measure contact angle on the images that were generated from the simulation data.[21] The image needs to be derived for each measurement and cannot be carried out on site, so the scheme is rough and time-consuming. For diffuse-interface simulations, Ding and Spelt[22] proposed a geometric formulation of wetting condition to measure contact angle. Lee and Kim[23] used a characteristic interpolation to improve accuracy and stability on this basis. Huang *et al.*[24] and Chen *et al.*[25] proposed an approximation for contact angle in the pseudopotential model, which achieves the field adjustable contact angle of nonlinearity and is verified by the spherical cap method. The spherical cap method is usually adopted to verify adjustable contact angle in the diffuse-interface simulations, and this method calculates the contact angle by using the bottom width and height of the droplet if it is small enough or the gravity is ignored. However, the gravity cannot be ignored in many cases. Wen *et al.*[26] proposed a geometry-based scheme to measure the contact angle at real-time, and the contact angle can be linearly adjusted by the chemical potential of the surface in the chemical-potential multiphase model. When the density ratio of gas phase to liquid phase increases, the accuracy of this scheme can be susceptible to the

[†]Corresponding author. E-mail: hebing@gxnu.edu.cn
[‡]Corresponding author. E-mail: oceanwen@gxnu.edu.cn

© 2023 Chinese Physical Society and IOP Publishing Ltd

interference of boundary conditions. In this work, we further improve the scheme to accurately obtain the contact angles at lower temperatures and larger density ratios.

The remainder of the paper is organized as follows. In Section 2, the chemical-potential multiphase lattice Boltzmann model is introduced. In Section 3, the improved scheme of contact angle measurement is described. In Section 4, the measurement accuracy and grid-independence are verified, and then the present scheme is used to capture the dynamical contact angle hysteresis and implement the mechanical analysis at the contact line. Finally, some conclusions are drawn from the present studies in Section 5.

2. Multiphase lattice Boltzmann method

One of the important applications for the lattice Boltzmann method is to simulate multiphase flow phenomena. With the discrete space, time and velocity, the multiple-relaxation-time lattice Boltzmann equation can be expressed as[29,30]

$$\begin{aligned} & f_i(x+\boldsymbol{e}_i\delta t, t+\delta t) - f_i(x,t) \\ = & -\boldsymbol{M}^{-1}\cdot\boldsymbol{S}\cdot[\boldsymbol{m}-\boldsymbol{m}^{(\mathrm{eq})}] + F_i, \end{aligned} \tag{1}$$

where $f_i(x,t)$ is the particle distribution function at time t and lattice site x, $\boldsymbol{e}_i$ is the discrete velocity vector and $i = 0,\ldots,N$. For the D2Q9 model, they are $\boldsymbol{e} = [(0,0),(1,0),(0,1),(-1,0),(0,-1),(1,1),(-1,1),(-1,-1),(1,-1)]$. F_i is the body force term, $\boldsymbol{m}$ and $\boldsymbol{m}^{(\mathrm{eq})}$ are the velocity moments of distribution functions and their equilibria respectively, $\boldsymbol{M}$ is a matrix that linearly transforms the distribution function into the velocity moment, $\boldsymbol{m} = \boldsymbol{M}\cdot\boldsymbol{f}$, where $\boldsymbol{f} = (f_0, f_1, \ldots, f_8)$ for the D2Q9 model, and $\boldsymbol{S} = \mathrm{diag}\left(0, s_\mathrm{e}, s_\varepsilon, 0, s_\mathrm{q}, 0, s_\mathrm{q}, s_\mathrm{v}, s_\mathrm{v}\right)$ is a diagonal matrix of relaxation times. In this study, the relaxation times are assigned by $s_\mathrm{e} = 1.64$, $s_\varepsilon = 1.54$, $s_\mathrm{q} = 1.9$, $s_\mathrm{v} = 1/\tau$.[29,31]

Since the Boltzmann equation assumes no correlation between particles prior to the collisions, the equation neither includes the nonideal effect nor describes the phase transition. The nonideal effect can be evaluated from the free energy principle. Following the classical capillarity theory of van der Waals, the free-energy functional within a gradient-squared approximation can be represented as

$$\Psi = \int \left[\psi(\rho) + \frac{\kappa}{2}|\nabla\rho|^2\right] \mathrm{d}x, \tag{2}$$

where the first term on the right-hand side is the bulk free-energy density with the density ρ, and the second term describes the contribution from density gradients in an inhomogeneous system, and κ is the surface tension coefficient. The general equation of state (EOS) and chemical potential are defined by the free energy density,

$$p_0 = \rho\psi'(\rho) - \psi(\rho), \tag{3}$$

$$\mu = \psi'(\rho) - \kappa\nabla^2\rho, \tag{4}$$

respectively. The nonideal force can be evaluated from the chemical potential

$$\boldsymbol{F} = -\rho\nabla\mu + c_\mathrm{s}^2\nabla\rho. \tag{5}$$

The phase transition induced by the nonideal force theoretically satisfies the thermodynamic consistency and Galilean invariance, which have been confirmed by numerical simulations of static and dynamic fluids.[32]

Solving Eq. (3), we can obtain the general solution of the bulk free energy density. The famous Peng–Robinson (PR) EOS is used to model the multiphase system

$$p_0 = \frac{\rho RT}{1-b\rho} - \frac{a\alpha(T)\rho^2}{1+2b\rho-b^2\rho^2}. \tag{6}$$

Substituting Eq. (6) into Eq. (3) and associating Eq. (4), the chemical potential of PR EOS is obtained to be[32]

$$\begin{aligned} \mu^{\mathrm{PR}} = & RT\ln\frac{\rho}{1-b\rho} - \frac{a\alpha(T)}{2\sqrt{2}b}\ln\frac{\sqrt{2}-1+b\rho}{\sqrt{2}+1-b\rho} \\ & + \frac{RT}{1-b\rho} - \frac{a\alpha(T)\rho}{1+2b\rho-b^2\rho^2} - \kappa\nabla^2\rho, \end{aligned} \tag{7}$$

where the universal gas constant $R = 1$, the attraction parameter and volume correction are $a = 2/49$ and $b = 2/21$ respectively, and the temperature function is $\alpha(T) = \left[1+\left(0.37464+1.54226\omega-0.26992\omega^2\right)\left(1-\sqrt{T/T_\mathrm{c}}\right)\right]^2$, where acentric factor ω is 0.344 for water. To relate numerical results to actual physical properties, we define the reduced variables $T_\mathrm{r} = T/T_\mathrm{c}$ and $\rho_\mathrm{r} = \rho/\rho_\mathrm{c}$, in which T_c is the critical temperature and ρ_c is the critical density. To improve the accuracy of the liquid–gas transition region, we use a suitable equation $\delta\hat{x} = k\delta x$, which establishes the connection between the lattice step δx of the momentum space and the mesh step $\delta\hat{x}$ of the computational mesh. The calculating results in the momentum space are translated into the mesh space by an optional proportional coefficient k. The chemical potential in the original Eq. (4) is rewritten as[33]

$$\hat{\mu} = k^2\psi'(\rho) - \hat{\kappa}\hat{\nabla}^2\rho, \tag{8}$$

where $\hat{\kappa}$ is the surface tension coefficient in mesh space. In this way, the original steep liquid–gas transition region will become gentler and get more details when the proportional coefficient is less than 1. The gentle transition region facilitates searching for the droplet interface with the geometry-based mesoscopic scheme and improves the accuracy of contact angle measurement.

The exact difference method proposed by Kupershtokh *et al.*[34] was used to incorporate the nonideal force incorporated into lattice Boltzmann equation as an external force, which is

simply equal to the difference between the equilibrium distribution functions before and after the nonideal force acting on the fluid during a time step

$$F_i = f_i^{(\mathrm{eq})}(\rho, \boldsymbol{u}+\delta\boldsymbol{u}) - f_i^{(\mathrm{eq})}(\rho, \boldsymbol{u}), \tag{9}$$

where $\delta \mathrm{u} = \delta t \boldsymbol{F}/\rho$. The macroscopic fluid velocity is redefined as the average momentum before and after the collision $\boldsymbol{v} = \boldsymbol{u} + \delta t \boldsymbol{F}/(2\rho)$.

3. Mesoscopic contact angle measurement

3.1. Chemical-potential boundary condition

In our simulations, the periodic boundary condition is used in the horizontal direction and the halfway bounce-back scheme is employed at the bottom boundary and top boundary. The surface wettability is adjusted by chemical potential, which is an essential parameter coupled to the density gradient. We further used the five-point central difference method[33,35] with fourth order accuracy to calculate the gradients, which involves 5 lattice nodes,

$$u_i' = \frac{4}{3}\frac{u_{i+1}-u_{i-1}}{2h} - \frac{1}{3}\frac{u_{i+2}-u_{i-2}}{4h}, \tag{10}$$

where u_i represents the density or chemical potential on the lattice node x_i, h is a lattice unit. Compared with the original three-point central difference method, the five-point central difference method is beneficial for calculating the density gradient. However, the five-point central difference method requires more neighboring nodes, which means that the substrate's chemical potential boundary condition needs two rows of solid nodes. The purple area represented the solid nodes ($y = 0$ and $y = 1$) in Fig. 1, their densities are calculated by neighboring nodes from the following equation:

$$\rho(x_\mathrm{s}) = \frac{\sum \omega_i \rho(x_\mathrm{s} + \boldsymbol{e}_i\delta_\mathrm{t}) s_\mathrm{w}}{\sum \omega_i s_\mathrm{w}}, \tag{11}$$

where ω_i is the weight of the corresponding direction in D2Q9 model, $x_\mathrm{s} + \boldsymbol{e}_i\delta_\mathrm{t}$ represents the adjoining nodes and s_w denotes a switching function. For the first layer of solid nodes ($y = 1$), if $x_\mathrm{s} + \boldsymbol{e}_i\delta_\mathrm{t}$ is a fluid node, $s_\mathrm{w} = 1$; otherwise, $s_\mathrm{w} = 0$. For the second layer of solid nodes ($y = 0$), if $x_\mathrm{s} + \boldsymbol{e}_i\delta_\mathrm{t}$ is the node appearing on the first layer, $s_\mathrm{w} = 1$; otherwise, $s_\mathrm{w} = 0$. On the other hand, the chemical-potential gradient reflects the interaction between the fluid and the wetting surface. The present model directly assigns a specific chemical potential to the solid nodes ($y = 0$ and $y = 1$). In this way, the five-point central difference method can be used to calculate the density gradient and the chemical-potential gradient.

3.2. Improved contact angle measurement

There are two problems to be solved in accurately calculating the contact angle. One is to find out the liquid–gas interface located exactly, and the other is to search for the location of the three-phase contact point. The liquid–gas interface is defined by the contour line where the density is equal to the mean density of the gas phase and liquid phase. This interface divides the liquid node and gas node in the transition region of the droplet. The liquid–gas transition region becomes gentler due to Eq. (8), the position of the droplet interface is easily obtained by the linear interpolation[26]

$$\boldsymbol{x} = \boldsymbol{x}_\mathrm{g} + \frac{\rho_\mathrm{m} - \rho_{(\boldsymbol{x}_\mathrm{g})}}{\rho_{(\boldsymbol{x}_\mathrm{l})} - \rho_{(\boldsymbol{x}_\mathrm{g})}}\boldsymbol{e}, \tag{12}$$

where $\boldsymbol{x}_\mathrm{l}$ and $\boldsymbol{x}_\mathrm{g}$ represent the liquid and gas node of liquid–gas link respectively; ρ_m is the average of the gas density and liquid density; $\boldsymbol{e}$ describes the direction from gas to liquid. The original measurement method seeks the three-phase contact point (black spot "a" in Fig. 1) on the first layer of fluid node ($y = 2$) by Eq. (12) as well as the interface of the droplet on the second layer of fluid node ($y = 3$). The contact angle can be determined by the line connecting these two points and the horizontal positive direction.[26] However, the density distribution of the first layer of fluid node ($y = 2$) adjacent to the substrate will tend toward the droplet center due to the influence of boundary condition. It leads the accuracy of the contact angle measurement to decrease.

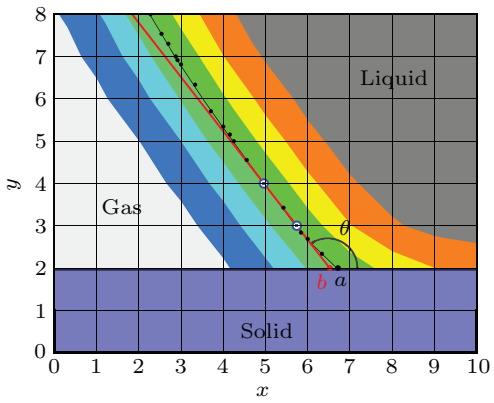


Fig. 1. Schematic diagram of three-phase region of droplet in substrate. Rainbow area is transition region of droplet, and black points are liquid–gas interface of the droplet. Black spot "a" represents three-phase contact point in previous method.[26] Two blue circles are intersections of liquid–gas interface and lattice lines. Red line passing through two blue circles intersects substrate at red spot "b", which is three-phase point in the present method.

In the present method, the interface of the droplet is still found by Eq. (12). We choose another two layers of fluid nodes ($y = 3$ and $y = 4$) for seeking the interface of the droplet (two blue circles in Fig. 1). These two layers of fluid nodes has a stable value due to the distance from the solid border. The three-phase contact point (red spot "b" in Fig. 1) is determined by linear extrapolation from these two blue circles. In this way, the extrapolated three-phase contact point will also have a stable value and not be affected by the boundary condition. It overcomes the deficiencies of the original method and further improves the accuracy of contact angle measurement. The contact angle is determined by the red line in Fig. 1 and

horizontal positive direction. The following simulation shows that the present method is more accurate and effective.

4. Simulation and discussion

A series of simulations is performed to verify the effectiveness of the improved contact angle measurement. Contrasting with the spherical cap method, the measurement accuracy of the droplet's contact angle on a horizontal surface is evaluated in an environment without gravity. Then, the grid independence of the present scheme is verified by changing drop sizes on different wetting surfaces. The dynamical contact angle hysteresis is captured to verify the real-time of the present scheme. Finally, because the microscopic contact angle reflects the mechanical equilibrium in the three-phase contact region, the present scheme is used to achieve mechanical analysis.

4.1. Verification of the measuring accuracy

In this subsection, droplets on a horizontal surface with a specific chemical potential are simulated, and the relations between contact angle of the droplet and chemical potential at multiple temperatures are analyzed. The computational domain is a rectangle with the length $Dx = 2000$ lattice units and the width $Dy = 500$ lattice units. The density of the flow field is initialized as follows:[36]

$$\rho(x,y) = \frac{\rho_{\mathrm{g}} + \rho_{\mathrm{l}}}{2} + \frac{\rho_{\mathrm{g}} - \rho_{\mathrm{l}}}{2} \tanh\left[\frac{2(r - r_0)}{W}\right], \tag{13}$$

where ρ_{g} and ρ_{l} are the gas and liquid coexistence densities obtained using Maxwell's equal area method,[37] and the initial interface width is $W = 10$. The initial radius of droplet is $r_0 = 60$ lattice units and $r = \sqrt{(x - x_0)^2 + (y - y_0)^2}$, where $x_0 = Dx/2$ and $y_0 = r_0 + 2$. Without gravity, the shape of the droplet on a horizontal surface is a spherical cap, and the contact angle is conveniently calculated by the droplet base L and height H. The radius of the droplet is calculated from $R_0 = (4H^2 + L^2)/8H$ and then the spherical cap method evaluates the contact angle from the formula $\tan\theta = L/2(R_0 - H)$.

Figure 2 shows the variations of contact angle with chemical potential, which are measured at temperature $T_{\mathrm{r}} = 0.7$ from hydrophilic surface to hydrophobic surface. Here a proportional coefficient k is 0.2 for the present method, while a proportional coefficient is not taken into consideration in the original method, specifically, k is set to 1. Thus, the liquid–gas transition region becomes gentler, the chemical potential for the same contact angle changes in the present model contrasting with the original model.[26] In Fig. 2, the upper axis and bottom axis represent the range of chemical potential for the original model and the present model, respectively. The results of the original mesoscopic measurement and spherical cap method are linearly related in general (see pink line and green line in Fig. 2). However, the contact angles that measured by these two methods are obviously bent when the droplet is located on the hydrophilic surface and superhydrophobic surface, which indicates that these two methods have limitations and deficiencies. In contrast, the contact angle that is measured by the improved scheme has a better linear relationship when it is less than 60° or larger than 165°. Meanwhile, we use the relative L_2-norm[38] to analyze the available results and verify the relative error of the two mesoscopic measurement methods. At the temperature $T_{\mathrm{r}} = 0.7$, the error of the original method is 0.0359, and the error of the improved method is 0.0121. This demonstrates that the present scheme is more accurate than the original one.

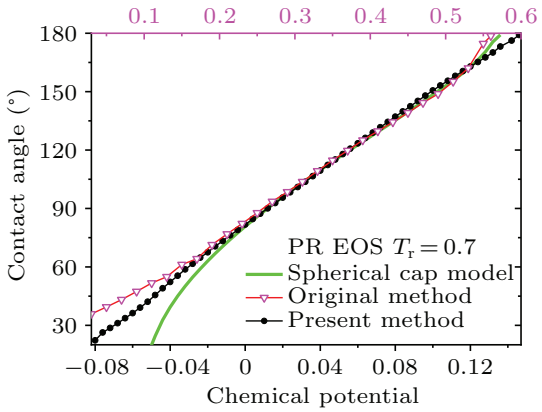


Fig. 2. Relationship between the contact angle and the chemical potential of substrate. Top axis is the chemical potential range of original method.[26] Temperature is $T_{\mathrm{r}} = 0.7$ and proportional coefficient is $k = 0.2$.

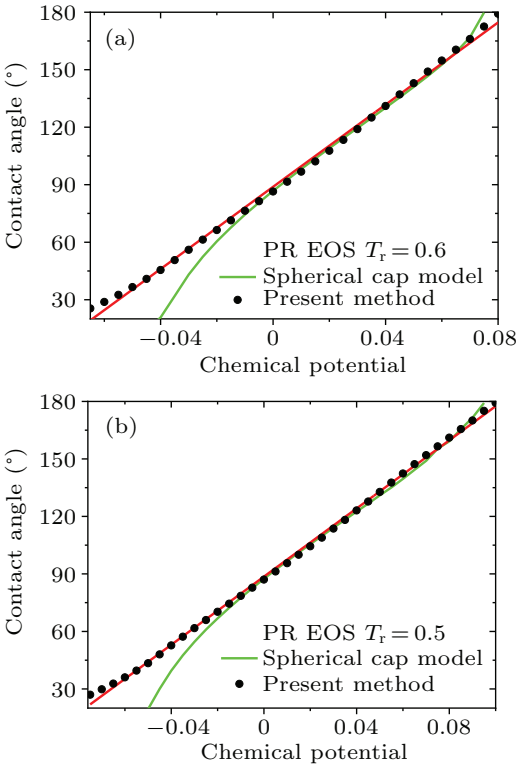


Fig. 3. Relationship between chemical potential of substrate and contact angle at (a) $T_{\mathrm{r}} = 0.6$, with density ratio being about 850, and (b) $T_{\mathrm{r}} = 0.5$, with density ratio being about 3200. Red line denotes result of black points linear fitting. Proportional coefficient is $k = 0.1$.

The present scheme can also obtain accurate contact angles at lower temperatures and larger density ratios. Figure 3 shows that the contact angle and chemical potential still have a nice linear relationship at $T_r = 0.6$ and $T_r = 0.5$. The liquid–gas phase density ratio is larger than 1000 in the natural environment. The liquid–gas phase density ratio in Fig. 3(b) is more than 3000, so the present scheme can measure the contact angle under larger density ratios. The nice linear relationship means that the method can adjust the surface wettability conveniently according to actual requirements.

4.2. Verification of grid independence

Verification of the grid independence is crucial in the results of numerical simulations. The contact angles of a series of droplets whose radii vary between 50 and 300 lattice units on five different wettability substrates are measured. As shown in Fig. 4, the contact angle measured by the present method is almost constant even though the radius of droplet keeps gradually increasing under the same chemical potential, which is consistent with the previous result.[26] We further analyze the results quantitatively, and the variance is about 0.2167. The results demonstrate that the present method is stable and grid-independent.

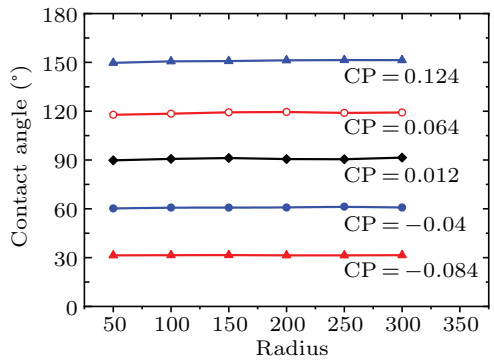


Fig. 4. Verification of contact angle independent of radius on wetting substrates, with proportional coefficient $k = 0.2$ and temperature $T_r = 0.6$.

4.3. Dynamic contact angle hysteresis

The roughness and chemical heterogeneity of the solid surface unavoidably lead to contact angle hysteresis.[39,40] In this subsection, we simulate a droplet on an inclined plate with alternant hydrophobic patterns and hydrophilic patterns to exhibit contact angle hysteresis. The contact angles on both sides of the droplet are asymmetric due to the effects of gravity and the slope angle of the plate. When the droplet slides along the inclined plate, the contact angle on one side that the contact line retracts to the inside of the droplet is called the receding angle θ_R, and another side is the advancing angle θ_A. As the slope angle of the plate gradually increases, the advancing angle grows and the receding angle decreases. It leads the advancing angle or receding angle to leave the initial position if the droplet is unstable. The simulations are applied to a chemically heterogeneous surface with a slope angle of 15°, whose hydrophilic region and hydrophobic region have the contact angles 60° and 120°, respectively. The initial droplet radius is $r_0 = 60$ lattice units and its macroscopic diameter is 0.06 cm. The droplet macroscopic density is 1 g/cm^3 and the gravitational acceleration is $|G| = 980$ cm/s^2.

Figure 5(a) shows the variations of contact angle hysteresis during the stick-slip motion of the droplet. It can be clearly seen that the contact angle hysteresis changes periodically between 0° and 60°. The reason for these variations is that advancing angle and receding angle have a time-phase difference when the droplet moves. In the droplet stick-slip motion period, the advancing angle θ_A appears as a trough, and the receding angle θ_R appears as a peak when corresponding three-phase contact line crosses the hydrophilic–hydrophobic junction. Meanwhile, the position of the three-phase contact line matches the position of the peak and trough well, which are shown by the orange line of Fig. 5(b) and the green line of Fig. 5(c). The improved scheme can also real-time measure the contact angle hysteresis from the simulation results.

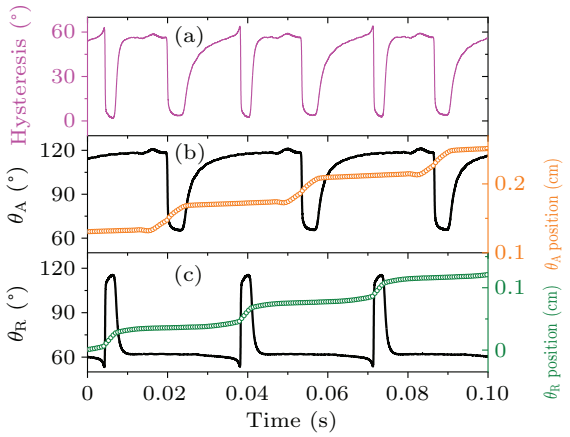


Fig. 5. Stick-slip motion of droplet on surface of alternant hydrophobic pattern and hydrophilic pattern, showing time-dependent (a) contact angle hysteresis, (b) advancing contact angle and its position, and (c) receding contact angle and its position.

4.4. Mechanical analysis on moving contact line

Mechanical analysis is an essential part of simulating the state of a droplet on an inclined substrate.[41] The deformation of the droplet in the three-phase contact region leads to the unbalanced Young's force, which (per unit length) can be expressed as[42,43]

$$F_u = \gamma\left(\cos\theta - \cos\theta_{eq}\right), \tag{14}$$

where γ represents the liquid–gas surface tension, and θ is the dynamic contact angle. In the case where the liquid–gas transition region is located on a homogeneous surface, θ_{eq} is the static contact angle of surface. If the liquid–gas transition region is located at the junction of the hydrophobic-hydrophilic

stripes, the equilibrium contact angle is evaluated from the modified Cassie–Baxter equation[43]

$$\cos\theta_{\rm eq} = r\varphi_{\rm d}\cos\theta_{\rm s1} + (1-\varphi_{\rm d})\cos\theta_{\rm s2}, \tag{15}$$

where $\theta_{\rm s1}$ and $\theta_{\rm s2}$ are the static contact angles corresponding to the two homogeneous regions, respectively. r refers to the roughness of the wetting surface ($r = 1$ for a smooth surface). In the context of two-dimensional diffuse interface model,[44] the width of the liquid–gas transition region can be described by the total length of the isodensity lines. Therefore, $\varphi_{\rm d}$ $(1-\varphi_{\rm d})$ refers to the ratio of the length of the isodensity line on the surfaces with contact angles of $\theta_{\rm s1}$ ($\theta_{\rm s2}$) to the total length of the isodensity lines.

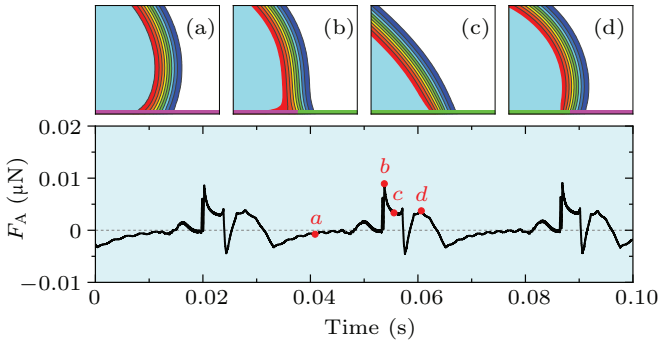


Fig. 6. Time-dependent unbalanced Young's force in advancing angle region, with purple line representing hydrophobic region, green line denoting hydrophilic region, and panels (a)–(d) showing contact line of the advancing angle region located at different positions.

In our simulation, mechanical analysis is conducted with the contact angle hysteresis at the same time. Therefore, the initialization parameters are the same as those in Subsection 4.3. Figure 6 shows the variation of unbalanced Young's force in the advancing angle region during the stick-slip motion of the droplet. When the three-phase contact line is located on a hydrophobic surface (see Fig. 6(a)), the unbalanced Young's force $F_{\rm A}$ in the advancing angle region gradually approaches to zero because the front part of the droplet turns back into shape after a sharp fluctuation, and fluctuates around zero. The advancing angle is affected by the depinning of the receding angle at this time, figure 6 shows that the $F_{\rm A}$ has a small peak at about 0.05 s, which also has a similar phenomenon to the counterpart in Fig. 5(b). Then, the contact line moves on the junction of the hydrophobic–hydrophilic regions (see Fig. 6(b)), which results in the deformation of three-phase contact region and the change of dynamic contact angle. Thus, $F_{\rm A}$ increases sharply in a short time. When the contact line continues to move to the hydrophilic surface (see Fig. 6(c)), $F_{\rm A}$ gradually decreases with the dynamic contact angle falling off. It is worth noting that the unbalanced Young's force exhibits a negative peak between spot "*c*" and "*d*" in Fig. 6 because the contact line experiences resistance from the hydrophobic substrate. The $F_{\rm A}$ goes in the opposite direction and the value is negative when the dynamic contact angle is less than the equilibrium contact angle in the advancing region of the droplet. Finally, the droplet enters into the next period when the contact line crosses the junction of the hydrophobic-hydrophilic regions (see Fig. 6(d)).

The variation of unbalanced Young's force $F_{\rm R}$ in the receding angle region is shown in Fig. 7, and its overall trend is similar to the counterpart in Fig. 6. When the receding angle region is located on a hydrophilic surface (see Fig. 7(a)), the contact line moves slowly and uniformly because the droplet gravity component and substrate resistance maintain the equilibrium of local force . The force $F_{\rm R}$ can stay at zero for a long time in this period. When the contact line crosses the junction of the hydrophilic–hydrophobic region, a sharp increase in dynamic contact angle leads to a change of $F_{\rm R}$. The rear contact line of the droplet slides quickly across the hydrophobic surface and enters into the next hydrophilic surface. The time of mechanics change matches the time at which the contact angle hysteresis occurs well. It indicates that the present method can measure dynamic contact angle and conduct the conduct mechanical analysis in real time.

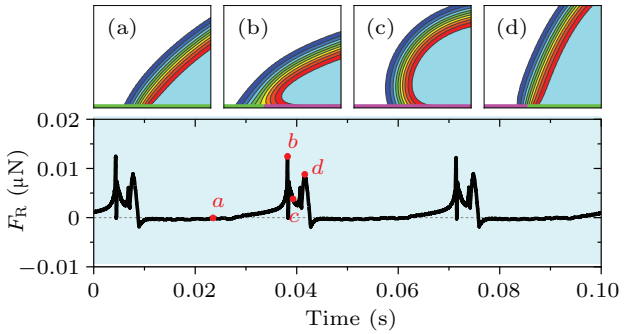


Fig. 7. Time-dependent unbalanced Young's force in receding angle region, with purple line representing hydrophobic region, green line denoting hydrophilic region, and panels (a)–(d) showing contact line of receding angle region located at different positions.

5. Conclusions

The contact angle is of great importance in simulating multiphase flow. In this work, the original geometry mesoscopic contact angle measurement is improved. The extrapolation method that finds the three-phase contact point overcomes the local deformation of the flow field in the three-phase contact region and further improves the accuracy of contact angle measurement. The results show that the method has good linearity and versatility, and effectively improves its accuracy . Verification of the grid-independence indicates that the improved measurement method can be applied to most droplet sizes. Since the present scheme is real-time, one can easily capture the dynamical contact angle hysteresis when a droplet moves on a chemically or physically heterogeneous surface.

Meanwhile, the microscopic contact angle reflects the mechanical equilibrium in the three-phase contact region, and the mechanical analysis is performed when contact angle hysteresis occurs. This scheme is expected to be used to measure the contact angle in complex multiphase flow field.

Acknowledgements

The authors thank the Guangxi Bagui Scholar Teams for Innovation and Research Project and the Guangxi Collaborative Innovation Center of Multisource Information Integration and Intelligent Processing for technical support.

Project supported by the National Natural Science Foundation of China (Grant Nos. 12272100, 81860635, and 12062005).

References

[1] Kwok D Y and Neumann A W 1999 *Adv. Colloid Interface Sci.* **81** 167
[2] Sui Y, Ding H and Spelt P D 2014 *Ann. Rev. Fluid Mech.* **46** 97
[3] Jopp J, Grüll H and Yerushalmi-Rozen R 2004 *Langmuir* **20** 10015
[4] Rayleigh L 1879 *Proc. R. Soc. London* **29** 71
[5] Bruel C, Queffeulou S, Darlow T, Virgilio N, Tavares J R and Patience G S 2019 *The Canadian Journal of Chemical Engineering* **97** 832
[6] Bigelow W, Pickett D and Zisman W 1946 *Journal of Colloid Science* **1** 513
[7] Extrand C and Kumagai Y 1996 *J. Colloid Interface Sci.* **184** 191
[8] Tretinnikov O N and Ikada Y 1994 *Langmuir* **10** 1606
[9] Alghunaim A, Kirdponpattara S and Newby B Z 2016 *Powder Technol.* **287** 201
[10] Washburn E W 1921 *Phys. Rev.* **17** 273
[11] Markodimitrakis I E, Sema D G, Chamakos N T, Papadopoulos P and Papathanasiou A G 2021 *Soft Matter* **17** 4335
[12] Zhou Y and Zhu P 2022 *The Innovation* **3** 100222
[13] Lin X, Yang F, You L, Wang H and Zhao F 2021 *The Innovation* **2** 100104
[14] Bachmann J, Ellies A and Hartge K H 2000 *Journal of Hydrology* **231–232** 66
[15] Brugnara M, Degasperi E, Volpe C D, *et al.* 2004 *Colloids and Surfaces A: Physicochemical and Engineering Aspects* **241** 299
[16] Mitchell B R, Klewicki J C, Korkolis Y P and Kinsey B L 2019 *J. Fluid Mech.* **867** 300
[17] Rankl M, Laib S and Seeger S 2003 *Colloids and Surfaces B: Biointerfaces* **30** 177
[18] Salaün F, Devaux E, Bourbigot S and Rumeau P 2009 *Text. Res. J.* **79** 1202
[19] Qin F, Zhao J, Kang Q, Derome D and Carmeliet J 2021 *Transport Porous Media* **140** 395
[20] Zhang Q, Sun D, Zhang Y and Zhu M 2014 *Langmuir* **30** 12559
[21] Benzi R, Biferale L, Sbragaglia M, Succi S and Toschi F 2006 *Phys. Rev. E* **74** 021509
[22] Ding H and Spelt P D M 2007 *Phys. Rev. E* **75** 046708
[23] Lee H G and Kim J 2011 *Comput. Fluids* **44** 178
[24] Huang H, Thorne D T, Jr., Schaap M G and Sukop M C 2007 *Phys. Rev. E* **76** 066701
[25] Chen L, Kang Q, Mu Y, He Y and Tao W 2014 *Int. J. Heat Mass Transfer* **76** 210
[26] Wen B, Huang B, Qin Z, Wang C and Zhang C 2018 *Comput. Math. Appl.* **76** 1686
[27] Sun D K, Jiang D, Xiang N, Chen K and Ni Z 2013 *Chin. Phys. Lett.* **30** 074702
[28] Zhang S, Tan Y D and Zhang S L 2014 *Chin. Phys. B* **23** 114202
[29] Lallemand P and Luo L 2000 *Phys. Rev. E* **61** 6546
[30] Lin C, Luo K H, Xu A, Gan Y and Lai H 2021 *Phys. Rev. E* **103** 013305
[31] Luo L, Liao W, Chen X, Peng Y and Zhang W 2011 *Phys. Rev. E* **83** 056710
[32] Wen B, Zhou X, He B, Zhang C and Fang H 2017 *Phys. Rev. E* **95** 063305
[33] Wen B, Zhao L, Qiu W, Ye Y and Shan X 2020 *Phys. Rev. E* **102** 013303
[34] Kupershtokh A, Medvedev D and Karpov D 2009 *Comput. Math. Appl.* **58** 965
[35] Qin Z R, Chen Y Y, Ling F R, Meng L J and Zhang C Y 2020 *Chin. Phys. B* **29** 34701
[36] Huang H, Krafczyk M and Lu X 2011 *Phys. Rev. E* **84** 046710
[37] Lebowitz J L and Penrose O 1966 *Journal of Mathematical Physics* **7** 98
[38] Wu F, Yang X H, Packard A and Becker G 1996 *International Journal of Robust and Nonlinear Control* **6** 983
[39] Eral H, Mannetje D and Oh J M 2013 *Colloid Polym. Sci.* **291** 247
[40] Gao L and McCarthy T J 2006 *Langmuir* **22** 6234
[41] Liang H, Liu H, Chai Z and Shi B 2019 *Phys. Rev. E* **99** 063306
[42] Li Q, Zhou P and Yan H J 2016 *Langmuir* **32** 9389
[43] He B, Qin C, Zhou S and Wen B 2020 *Phys. Rev. Fluids* **5** 114003
[44] Anderson D M, McFadden G B and Wheeler A A 1998 *Ann. Rev. Fluid Mech.* **30** 139